Long-term ionospheric cooling: dependency on local time, season, solar activity and geomagnetic activity

Shun-Rong Zhang and John M. Holt

Haystack Observatory, Massachusetts Institute of Technology, Westford, Massachusetts

J. M. Holt and S.-R. Zhang, Haystack Observatory, Massachusetts Institute of Technology, Route 40, Westford, MA 01886. (shunrong@haystack.mit.edu)

Abstract. This analysis of long-term Ti trends in the F-region over different local times is based on a database of incoherent scatter radar (ISR) observations spanning more than 3 solar cycles during 1968-2006 at Millstone Hill, and represents an extended effort to a prior study focusing on noontime only [Zhang et al., 2011]. This study provides important information for understanding the difference between the ISR and other results. A gross average of the Ti trend at heights of Ti∼Tn is ∼ (200-350km) -4K/decade, a cooling trend close to the Tn estimation based on the satellite neutral density data. However, there exists considerable variability in the cooling: it is strong during the day and very weak during the night with a large apparent warming at low altitudes (200-350km); it is strong at solar minimum for both daytime and nighttime. The strongest cooling for altitudes below 375 km occurs around 90-120 solar flux units of the 10.7 cm solar flux, not at the lowest solar flux. There appears more cooling toward high magnetic activity, but this dependency is very weak. No consistent and substantial seasonal dependency across different heights was found. We speculate that a fraction of the observed cooling trend may be contributed by a gradual shifting away from the sub-auroral region at Millstone Hill, as part of the secular change in Earth's magnetic field. In this 39-year long series of data record, two anomalous Ti drops were noticed, and we speculate on their connection to volcano eruptions in 1982 and 1991.

1. Introduction

If greenhouse gas concentrations are doubled, as predicted to happen by the end of the 21st century, Roble and Dickinson [1989] and Qian et al. [200] indicated that the decrease in thermospheric temperature will be as much as 50 K, and the decrease in thermospheric densities at a fixed height will be 40-50%. Observations of thermospheric total mass density by satellites revealed a 2-5% decrease per decade [Keating et al., 2000; Emmert et al., 2004; Marcos et al., 2005; Emmert et al., 2008], and have been considered as evidence of thermospheric cooling. The ionospheric consequence of thermal contraction includes a decrease in the F2 peak height [Rishbeth , 1990], a decrease in the topside ionospheric density [Zhang et al., 2011] and an increase in the F1 and E region ionospheric densities (e.g., Bremer [2008]). Progress has been made in identifying and understanding upper atmospheric trends in various observations in the past two decades, and is reviewed recently by, e.g., Qian et al. [2011]; Cnossen [2012]; Danilov [2012]; Laštovička et al. [2012].

The greenhouse gas effect, however, may not be the sole reason for the observed secular changes in the ionospheric and thermospheric parameters. Long-term changes in both solar and geomagnetic activity [Mikhailov and Marin, 2001], and secular variations of the geomagnetic field [Yue et al., 2006; Cnossen and Richmond , 2008] are other drivers that have been suggested to cause long-term changes in the upper atmosphere. More recently, W. L. Oliver et al. (W. Oliver, S.-R. Zhang, and L. Goncharenko, Is global thermospheric cooling caused by gravity waves? submitted to J. Geophys. Res., 2013) have proposed a new mechanism for the observed upper atmospheric cooling as caused by the long-term enhancement of gravity wave activity, which resulted from ocean-atmosphere interaction and wave propagation into the thermosphere

The upper atmospheric temperature is a key to understanding variations in the ionosphere and thermosphere. A drop in the neutral temperature can cause corresponding changes in the neutral composition and circulation (winds), therefore affecting ionospheric density through photo-ionization, chemical loss, diffusion and dynamics. The ground based incoherent scatter radar (ISR) can provide long-term and continuous monitoring of the upper atmospheric thermal status; radar observations of plasma temperatures and densities can be even used to derive neutral temperature and composition [Bauer et al, 1970; Oliver, 1979]. In particular, ion temperature (Ti) is very close to neutral temperature (Tn) at heights below the F2 peak, and features a well-defined high positive correlation with the solar 10.7 cm flux, the proxy F107, which allows to easily separate effects of the solar activity on long-term trends. Altitude profiles of the radar measured ionospheric/thermospheric parameters contain crucial information for understanding varying relative roles of factors perhaps associated with long-term changes in the main part of the ionosphere.

In an initial attempt to prove a direct measure of the upper atmospheric temperature trend, Zhang et al. [2005b] identified a negative Ti trend for most F2 region altitudes and seasons above Millstone Hill over 1978-2002. Holt and Zhang [2008] showed a long-term cooling rate of -4.7K/year in Ti with a 95% confidence interval of -3.6 to -5.8K/year at noon for 375 km, based on Millstone Hill ISR data for the period of 1978-2007. Using a similar Millstone Hill ISR data set but for the 100-500 height range over nearly 40 years in 1968-2006, Zhang et al. [2011] provided the noontime height profile of the Ti trend. The cooling was found to grow increasingly into the topside, stay less changed at 200-250 km, and show apparent warming in the E and F1-region. The noontime cooling is more significant at low solar activity than at high solar activity. These results appear qualitatively similar to the cooling trends from the theoretical modeling [Qian et al., 2011; Akmaev et al., 2006; Roble and Dickinson, 1989]. The Millstone Hill electron temperature (Te) shows a warming trend [Zhang et al., 2011], the Millstone Hill electron density (Ne) shows an increasing trend in the E-low F region and a decreasing trend above the F2 peak, with minor changes around the F2 peak, all of which agree with speculation based on long-term cooling in the upper atmosphere.

Donaldson et al. [2010] used St. Santin ISR data to examine Ti trends during a two-solar cycle period (1966-1987), and a significant cooling trend was revealed in the topside ionosphere. They also indicated the local time dependency of the trend, being larger during the day than at night. It should be noted that the St. Santin data set covered only up to 1987 when the global warming signals in the ground/low atmospheric temperature just emerged. The so-called trend "breakpoint" in the early 1980s was noticed from these radar and other observations [Danilov, 2008; Walsh and Oliver, 2011; Zhang et al., 2011] and its connection to a plausible O_3 influence [Akmaev et al., 2006] was initially speculated by Walsh and Oliver [2011] but then disputed by Laštovička [2012].

This paper addresses variability in the Ti trend as measured by the Millstone Hill radar, and discusses plausible causes for the observed variability. In addition to the height dependency of the trend, we will resolve the diurnal variation of the trend, and determine the diurnal average trend based upon data from different local times of the day. We will also examine the seasonal, solar activity and magnetic activity dependency of the diurnal average trend. This work updates what has been shown in Zhang et al. [2011] for the noon-time only result. These new results are particularly important when one attempts to make direct quantitative comparisons between ISR observations and the global means from model and satellite observations [Cnossen, 2012; Akmaev, 2012]; these global means were calculated typically using data with different local times. As it turns out, some of the quantitive discrepancies may be ascribed to variability in the temperature trend, in addition to other factors.

2. Data and Method

Detailed description on the long-term observational dataset from the Millstone Hill ISR, as well as trend-detecting method were given in Zhang et al. [2011]; here we highlight only some significant aspects, in particular, those different from the previous work.

While the previous work by Zhang et al. [2011] focused on noontime data only, the current work deals with data from different local times. Typically, nighttime measurements are fewer than during the daytime, especially in the E region where the volume of nighttime observations suited for detecting subtle long-term trends is insufficient. We therefore opt to the F-region observation (i.e., 200-500 km). As in the previous work, we concentrate on the zenith antenna observations of the radar from the year 1968 through the end of the year 2006. More recent data have not been included in the analysis to avoid complication caused by the recent extended solar minimum [Emmert et al., 2010].

Data distribution statistics for Ti measurements within 200-550 km is shown in Figure 1. These are the measurements that will enter into the next step of monthly median calculation after binning in height and local time, with obvious bad-data and outliers removed. The top panel (a) shows counts of observational points in log_{10} units as a func- **Figure 1** tion of year and UT. The mid-panel (b) shows the data counts in log_{10} as a function of year and month. On average, for any given local time, month, year, and height bin, there are 30-40 qualified data points that enter into the statistics, or for any given local time and year (regardless height and month) 3,500 data points (panel a), for any given month and year (regardless height and local time) 4,600 data points (panel b), and for any given local time and month (regardless height and year) 13,000 data points (panel c). There were relatively more data points in the later years (since 1990s) than in the earlier years; in the later years, there were more data during the day than at night. The three months, March, September, and October, have many more data points, and this was due to the three month-long campaigns during October 2002, September 2005 and March 2006 [Zhang et al., 2005a; Zhang and Holt, 2008]. Therefore calculating the monthly median is an important procedure to effectively avoid the oversampling issue.

The data are first binned into 24 local time subsets, each corresponding to observations within 1 hour local time. This will allow us to derive the diurnal variation. The subsequent procedure is the same as described in Holt and Zhang [2008] and Zhang et al. [2011]: the data in a given local time subset is further binned according to height, with a 50 km bin size. For a given height and local time bin, a monthly median is found if the number of data points is greater than 6. Taking monthly median values allows us to eliminate outliers, over-sampling issues for some of the months, and short-term (hours or days) auto-correlation. This binning and averaging process results in the Ti dataset shown in Figure 2, where each point corresponds to a monthly median for a given local time bin and altitude bin. The associated F107 and Ap indices are also included. Solar cycle

Figure 2

and seasonal variations in Ti can be easily seen. Data with F107 > 300 or Ap > 80 are eliminated to minimize effects from extreme solar-geophysical conditions.

The long-term trend is then determined for each local time-height bin based on these monthly means through least-squares fitting to a model including terms of background constant, solar flux, magnetic activity and the long-term trend. This model takes the following form:

$$\begin{aligned} T_i &= T_b + t(y - \bar{y}) \\ &+ f_1(F107 - \overline{F107}) + f_2(F107 - \overline{F107})^2 \\ &+ a(Ap - \overline{Ap}) \end{aligned} \qquad (1)$$

where y is the floating-point year containing day number of the year information in the floating-point, $\bar{y}$ is the mean floating-point year, F107 is the daily solar 10.7 cm flux, $\overline{F107}$ is the mean F107 determined over the entire time span, Ap is the daily Ap index, and $\overline{Ap}$ is the mean Ap value determined over the entire time span. The background constant term T_b, long-term trend t, and F107 and Ap term coefficients f_1, f_2 and a are obtained through least square fitting for each local time-height bin. Currently the model does not include cross terms but gives simple and straightforward dependencies. Results shown in the later sections, in particular variabilities with F107 and year, may imply effects of these cross terms which we may pursue in the future.

The monthly data may be decomposed into various components of variation as shown in Figure 3. The decomposed data are residuals, for instance, the trend residuals (left panel) are calculated by subtracting regression values with all terms except for the trend one (i.e., background, solar activity and magnetic activity terms from the monthly means) for a given height bin and each of the 24 hourly bins. These trend residuals are the primary

Figure 3

data we will be examining in the following sections. The diurnal, seasonal, yearly, and long-term variations are indicted by the gray dots. In this panel, the red line is the linear trend determined based on these data points. The yearly averaging over all hours of the day and all seasons of the year is also performed in order to characterize year-by-year variations; these results are indicted by the blue dots. The F107 residuals (middle panel), however, are calculated by subtracting regression values with all terms except for the F107 terms. These data from each hour of the day, each season and each year are given by the gray dots. A linear fit to them is shown by the red line, while a parabolic fit to them is also given by the yellow line. The two fits are essentially the same for F107 $<$ 250 sfu (solar flux unit, $10^{-22} W m^{-2} Hz^{-1}$, hereafter we drop "sfu" to treat F107 as a dimensionless index). This plot shows the overall good linearity of the Ti-F107 dependency for F107 $<$ 250. This is somewhat different from the midday only situation where a parabolic function fits data better due to the saturated response in Ti for high F107 [Zhang et al., 2011]. Similarly, the Ap residuals (right panel) are calculated by subtracting regression values with all terms except for the Ap one for a given height bin and each of the 24 hourly bins. The positive correlation between Ti and Ap is a very significant feature, and as a first order approximation, they exhibit primarily a linear relationship which can be seen by the red line.

3. Result and discussion

We now present results for the Ti trend residuals, derived after removing solar and magnetic activity influences as described in the last section. The overall feature can been seen on the left panels in Figure 3 and a number of turning points may be summarized in the chronological order as the follows: (1) A positive temperature spike near the year

1976, being more significant for > 350 km. (2) A clear drop in the year 1982, being more prominent at low altitudes. (3) Another drop centering the year 1993. (4) A fairly large drop around the year 2004. We do not fully understand these spikes and drops, which are residuals after subtracting solar cycle and magnetic activity influences. However, it seems that some of these drops (in 1982 and 1993) in Ti are possibly correlated to volcano activities. This will be further addressed in Section 4.2.

In the following subsections, we will describe trend variability with height, local time, season, solar activity and magnetic activity. These characteristic variations are based on trend residuals, with background constant, solar and magnetic activity terms removed.

3.1. Diurnal and height variations

The long-term trend in Ti exhibits a distinct day-night difference. Here we define daytime hours as 12±4 LT and nighttime hours 00±4 LT. Figure 4 shows the trends derived with a least square linear fitting using daytime, nighttime and all (24 hourly) residual data respectively (the left panel). Standard deviation error bars for the trend fitting are given also. Both daytime and nighttime trends show an increasing cooling with height, however, the cooling during the day is stronger and overwhelming throughout the F2 region height. At 225 km and 275 km heights where Ti is considerably close to Tn, the daytime cooling is -0.749 ± 0.131 K/year, -1.416 ± 0.144 K/year, respectively. The nighttime trends, however, are cooling above 350 km and warming below 350 km, with a maximum apparent warming of +1.624 ± 0.191 K/year at 275 km. The apparent warming at fixed heights does not necessarily mean a true warming in the upper atmosphere; a downward shift in the pressure level that is initiated with a large cooling at low altitudes can cause an apparent warming, because of subsidence of the warmer air with a substantial

Figure 4

height gradient in temperature as is the case for the low F region [Akmaev and Fomichev, 1998; Donaldson et al., 2010; Zhang et al., 2011]. This apparent warming is observed at very low altitudes during the day (see also Zhang et al. [2011]), and at higher altitudes at night. The large cooling in the underlying atmosphere needed to cause this apparent warming includes, among other possibilities, the CO_2 long-term cooling with additional contributions from O_3 cooling [Akmaev, 2012]. However, the observed apparent warming appears sometimes (at night) around the F2 peak height, well above the E region or the E-F1 region heights indicated by these CO_2 and O_3 based modelings.

It is interesting to note that the weak cooling trend at night comes along with the absence of solar irradiation. During the day, the cooling caused neutral density decrease can lead to less absorption of the solar EUV energy, even though the optical depth is increased. Based on the reduced energy absorption, the thermal balance may lead to a lower thermospheric temperature. During the night, however, this extra reduction in energy absorption from the solar EUV irradiation does not take place, and therefore a weak cooling trend may be expected. Further more, the height gradient in the neutral temperature depends very much on thermospheric temperature and on absorption of solar heating at low altitudes where neutral densities are high, and therefore subsidence of the warmer air may be more significant at night with the absence of solar heating and cause stronger apparent warming.

The variation of the trend between the daytime and the nighttime is gradual as shown in Figure 5. Below 350 km, the sharp day-night difference with a characteristic apparent **Figure 5** warming at night starts to emerge between 0500-0800 LT in the morning, being earlier at higher altitudes, and between 1800-2000LT in the afternoon, being later at higher altitudes. The timing of the day-night transition in the cooling trend intensity is compatible with the speculation based on the day-night transition of solar irradiation influence mentioned above.

As a result of day-night difference in the cooling trend, the diurnal average cooling is lower than the daytime one and higher than the nighttime one. This average cooling is at a rate of -0.044 ± 0.101 K/year for 225 km, -0.159 ± 0.101 K/year for 275 km, -0.857 ± 0.100 K/year for 325 km. In other words, the Millstone Hill ion temperature reduction over the 39 year period from 1968-2006 is -1.73K at 225 km, -6.21K at 275 km, and -33.4K for 325 km. These values are much smaller than, or nearly half of, those derived for noontime only data reported in Zhang et al. [2011]. Akmaev [2012] estimates a 4-6K/decade neutral temperature decrease between 200-400 km based on the observed neutral density trend; for comparison, our Ti average over 225 km, 275 km and 325 km, which are altitudes of Ti∼ Tn, is -0.3533 K/year or -3.5K/decade.

At higher altitude (>350km), where Ti>Tn, the diurnal average trend is -15.5K/decade at 375 km and -28.0K/decade at 425 km. In comparison, Holt and Zhang [2008] gave a -47K/decade trend for midday at 375 km (in years 1978-2007); the apparent deviation from the trends in the current study arises largely from the characteristic diurnal variation in the trends. Ti trends for these heights, however, may be different from Tn trends. In fact, Ti is biased typically by ∼70 K from Tn at midday in spring for median solar activity at 350 km. This bias is determined by neutral density, electron (ion) density and electron temperature, because the F region ions are primarily heated by electrons through Coulomb collisions, and cooled by elastic collisions with the neutrals, as indicated in a very simplified energy balance equation for the ions (O^+) [Bauer et al, 1970], $aN_eN_i(T_e - T_i) = bN_iN_O(T_i - T_n)$

where a and b are collision frequency related terms, N_i ion (O^+) density and N_O oxygen density. The Ti and Tn separation depends very much on neutral density for the same amount of electron heating: the less the N_O density (as a result of long-term cooling, for instance), the larger the Ti and Tn separation inclines to be. On the other hand, the less the electron density, the less energy the ions can gain and the greater the ion and electron temperature separation is, as demonstrated in Zhang et al. [2004]. The long-term reduction in the topside ionospheric electron density, associated with the long-term cooling (plasma/neutral scale height reduction), was shown in Zhang et al. [2011]; this electron density reduction may lead to less energy transfer to the ions from electrons. Therefore the long-term decrease in Ti is a combined result of increased cooling of the ions by the neutrals and decreased energy transfer from electrons to the ions and neutrals. The latter effect is less important at low altitudes due to the dominance of close thermal coupling between the neutrals, ions and electrons. Detailed quantitative calculations will help understand the trend difference between Ti and Tn, but a relevant consequence of the same long-term electron density reduction at the topside has been seen as the Te enhancement. This was on the order of +20K/decade as evidenced in Zhang et al. [2011].

3.2. Seasonal variation

Seasonal variation can be obtained by sorting data with different local times and years according to month (or day number of the year). Figure 6 gives seasonal variation of the trends at 4 altitudes and the corresponding median Ti. The seasonal bin size is 3 months. Ti exhibits clear and simple annual variations with higher temperatures in summer between May and July, and lower temperatures in winter. The trend, however, is less variable over the year, especially, at lower altitudes than at higher altitudes. At

Figure 6

high altitudes, the cooling is slightly stronger in April, and weaker in winter and summer months. Only at above 375 km can semiannual variations be seen with less cooling in winter and summer month, and more cooling in equinox, but reasons for more cooling in equinox (especially in April) remain unknown. Overall, seasonal variations in the Ti trend are negligible and this conclusion is similar to what was noted in the noontime data in Zhang et al. [2011]. These results of a negligible seasonal dependency are in agreement with those from the neutral density trends given by satellite measurements [Emmert et al., 2004].

3.3. Solar activity dependency

The solar activity dependency of the long-term trend in the upper atmosphere has been recognized as a profound feature with cooling and the related neutral density decrease being stronger at low solar activity than at high solar activity [Emmert et al., 2008; Zhang et al., 2011]. We confirm this feature based on our 24-hour dataset. Figure 7 provides **Figure 7** profiles of trends derived from the trend residuals with F107<130 (low solar activity) and with 130 <F107<180 (high solar activity), respectively. The cooling trend at low solar activity is enhanced by more than 2K/year from that at high solar activity, consistently throughout the 200-550km height range. An apparent warming appears strongly in the whole-day average trend at high solar activity. This is primarily caused by the enhanced apparent warming at night. Considering daytime only data (12±4LT; solid lines in the figure), the apparent warming disappears and the trend is very close to zero at low altitudes. This time dependent difference between solar activities is illustrated in Figure 8 **Figure 8** where the Ti trends as a function of height and local time are compared for the two levels of solar activities. The apparent warming exists at night for high solar activity.

So far our analysis has classified data into two levels of solar activity. Now to examine closely the solar activity dependency in more detail, we group trend residual data into fine F107 bins based on availability of observations shown in the F107 histogram in Figure 9 (upper panel). It is interesting to note that this is not a normal distribution where most of available F107 data is close to its median value. Instead, observations for low solar activity were confined to a small range of F107, in particular, between 70 – 90 where the number of observations is very high. On the other hand, observations at high solar activity show a very long tail from 135 – 240 . The fine F107 bins as illustrated in the bottom of the top panel are designed to be roughly equal in the number of data points, with their central F107 values meaningfully distributed so that these bins are distributed narrower for low solar activity and wider for high solar activity. The variation of the trends as a function of F107 shows little variability with height. They decrease (more cooling) with increasing F107 till F107=90–100 is reached, then they increase rapidly (weak cooling) with F107 further increasing, and the least change (close to a 0 trend) is observed at ∼130 . Within 200 > F107 > 125, the trends stay roughly constant, being less cooling.

Figure 9

Because of the apparent warming that occurs at low altitudes during the nighttime, more strongly toward high solar activity, as noted earlier, the daytime and the whole-day average trends start to behave somewhat differently for F107 beyond 125. In particular, when F107 runs from 180 to 250, the whole day trend stays fairly stable while the daytime cooling enhances toward higher solar activity. Due to the number of data points, the uncertainty for the estimated trend at F107=250 is large. In summary, this analysis shows an expected feature of more cooling at low solar activity than at high solar activity, however, a deep cooling around 90-125 of F107 is unusual and contributes significantly to the overall strong cooling at low solar activity.

The CO_2 infrared emission at 15 μm is the dominant cooling mechanism of the thermosphere above 100km among the three key ones, the other two being NO emission at 5.3 μm and the fine structure emission line of oxygen at 63 μm. Two important aspects of the NO cooling should be noted [Qian et al., 2011]. (1) NO radiative cooling tends to mitigate the CO_2 cooling effect: the enhanced CO_2 cooling rate (due to a long-term CO_2 concentration enhancement in the underlying atmosphere) at ~110 km is accompanied by the reduced NO cooling rate at ~ 150-200 km. This is because the reduction in neutral densities (caused by the enhanced CO_2 concentration), including NO and O, can cause the NO cooling rate decrease. (2) The importance of NO cooling, relative to that of CO_2 cooling, in governing the thermospheric temperature structure is not ignorable at solar maximum, because of the substantial increase in the NO cooling rate [Marsh et al, 2004]. NO density is high at solar maximum and low at solar minimum . The excited nitrogen, which reacts with molecular oxygen to produce NO, comes primarily from energetic electrons impact and NO^+ dissociation recombination. They both increase with increasing solar activity. As a result, at solar minimum, the CO_2 cooling is relatively more important than the NO cooling.

These results shown in Figures 7 and 8 are based on trend residuals, which are determined by subtracting from data all dependencies except for the long-term trend, as indicated in Equation (1). In particular, the solar activity dependency is expressed as the two F107 terms. The question is then whether the NO cooling effect has been effectively removed using the F107 terms in this equation. If the answer is yes, our residual trend data should not be subject to the substantial solar activity variability caused by the NO effect. The enhanced solar activity can cause enhanced NO cooling, implying a potential negative correlation between solar activity and temperature, whereas both neutral and ion temperatures can also increase with increasing solar activity to respond to the enhanced solar EUV flux, implying a positive correlation. These two competing processes work to cancel effects from the other to some degree. But overall, as indicated in Figure 3, there appears a strong positive correlation. Therefore these terms are considered as the first order effect, and the dependency of the trend residuals on F107 shown here represents a secondary effect, perhaps involving contributions from multiple competing factors.

The nonlinearity, shown as the deepest cooling for F107 between 90-125 and weak cooling for F107<90, may be also due to the failure of the F107 index to be a good solar EUV flux proxy at extremely low solar activity. For instance, the F107 index can overestimate the solar EUV effect on the thermospheric density, as was the case for the recent extended solar minimum [Emmert et al., 2010; Solomon et al., 2010, 2011], or the very low F107 index gives Ti higher than it should be, and therefore the corresponding residual trend will be lower, or more cooling, which seems to be opposite to our results here where we see less cooling toward the low end of F107. Detailed knowledge on the solar EUV and F107 index within a whole spectrum of F107 range is desired to clarify the observed nonlinearity in the temperature trends.

Projecting this non-monotonic trends-F107 relation into the trends-year relation, we may find decadal fluctuations about the trend line (Figure 3). These fluctuations differ from solar cycle variation and may possibly suggest influences by additional factors.

3.4. Magnetic activity dependency

The magnetic activity control on the upper atmospheric thermal status is complicated, however, since we are primarily focusing on less stormy conditions with Ap $\leq$ 80, a linear relationship between Ti and *Ap* may be assumed as in the MSIS models [Hedin, 1987], and can be seen in Figure 3. The trend residuals for Ap<30 and for Ap=[20 80] are analyzed to derive long-term trends for very quiet and moderate magnetic activity conditions (Figure 10). We can see that the cooling is more significant consistently throughout all heights, by more than approximately 1-2 K/year, for higher magnetic activity than for lower magnetic activity. Proceeding as we did with F107 (as in Figure 9), we obtain the magnetic activity dependency based on 4 groups of Ap indices (Figure 11). A somewhat monotonic relationship between Ap and the trends can be identified: we can see that cooling is gradually enhanced toward high magnetic activity.

Figure 10

Figure 11

A long-term increase in magnetic activity over the 20th century was indicated in some previous studies (e.g. Clilverd et al. [1998]; Mursula and Martini [2006]). Can such an increase, if true indeed, cause a long-term cooling based on our observed Ap increasing and Ti cooling correlation for the 1968-2006 time span? It is not immediately clear that the thermosphere-ionosphere behavior and magnetic activity during 1968-2006 are representative of those over the entire last century. There are additional problems: firstly, it is hard to imagine that the upper atmosphere as a whole can be cooled with more incoming solar energy inputs in the form of the enhanced magnetic activity; the observed cooling trend may not be explained in term of secular magnetic activity changes unless we can assume that appropriate energy transfer takes place between high and and low latitudes or between high and low altitudes. Secondly, the magnitude of increase in magnetic activity over the time frame (1968-2006) of our observations is rather weak. The Ap index, with an average of 14.5, drops at a rate of -0.018 /year, or by less than 1 Ap unit over the entire time span. This is simply too tiny. As shown in Figure 11, for Ap$\leq$30 where the trend dependency is most strong, the rate of change in the trend is approximately -0.06 K/year per Ap unit for 325 km. Thus this analysis suggests that secular change in the magnetic activity does not seem to be strong enough to account for the observed cooling trend in the upper atmosphere.

4. Further discussion

These characteristic variabilities in the trend demonstrated the complexity of the upper atmosphere system in modifying forcing from the atmospheric long-term change. One further plausible cause among those suggested drivers possibly responsible for the trend is a secular change of the Earth's magnetic field. This section will examine this effect. We will also explore a possible connection between volcano activities and the ionospheric temperature drops.

4.1. Secular changes in the magnetic field

At 300 km altitude over Millstone Hill, within the last 40 years from 1965-2005, the corrected geomagnetic (CGM) latitude decreased by 2.9° from 54.9 to 52.0°N, the Apex latitude decreased by 2.8°, the dipolar latitude decreased by 5.4°, and the the magnetic inclination angle decreased by 3.6°. These calculations are primarily based upon the IGRF2010 model [IAGA Working Group V-MOD, 2010]. They indicate that Millstone Hill is shifting away from its sub-auroral type location to be more mid-latitude in a very tangible way. This means that Millstone Hill is becoming less directly affected by the solar and magnetosphere events where precipitating energetic particles and enhanced electric fields can bring about heating on the neutrals and accelerate the ions, among other consequences. Much of the observed Ti variability at Millstone Hill has its origin in small fluctuations of magnetic activity, as reported in Zhang and Holt [2008] for a variability study based on a month-long campaign of ISR observations. Therefore, the secular change in the magnetic field is a potential factor for the observed long-term cooling in Ti over Millstone Hill.

To quantify this effect, we select results specifically for Millstone Hill from a global simulation performed by Cnossen and Richmond [2013]. In that simulation, the Coupled Magnetosphere-Ionosphere-Thermosphere (CMIT) model [Wang et al., 2004; Wiltberger et al., 2004; Wang et al., 2008] was employed. Simulations with the magnetic field of 1958 and 2008 as specified by the IGRF model [IAGA Working Group V-MOD, 2010], were carried out to investigate upper atmospheric changes associated with the use of different magnetic fields. The two runs were for a period of 15 days, from 0 UT on 21 March to 0 UT on 5 April, and used the solar wind conditions for that time interval in 2008. The solar activity level was also set to the level in 2008. Therefore these runs allow for some day-to-day variability near spring equinox at solar minimum. The day-to-day variability is of course very large and the signals from magnetic field changes can be better viewed based on the means obtained over each of the two 15-day periods. These means are typically with an standard deviation uncertainty of 30K. The difference of the calculated mean Ti between 2008 and 1958 magnetic field scenarios is shown as a function of local time and height in Figure 12. The blue color in the figure indicates a Ti decrease throughout most of the local times and heights, indeed an expected cooling trend. The cooling grows as **Figure 12** a function of height, stronger during the day, somewhat similar to observations shown in Figure 5. The magnitude of cooling is ∼-2K at around 250 km (and up to 10K at 400 km). This change over 50 years can be translated into approximately -0.4K/decade, which accounts for ∼8% of the observed ∼ -4K/decade cooling over 1968-2006. Due to the large day-to-day variability in simulation, the amount of cooling given here remains to be a very coarse estimate.

4.2. Connections to volcano activity?

During the time period of 1968-2006 of interest to the paper, there were 4 major volcano eruptions with a vocalic explosivity index (VEI) up to 5. VEI provides a measure of the volcanic eruption magnitude [Newhall and Self, 1982]. This logarithm scale index is open-ended with the largest volcanic eruptions in history given magnitude 8. A value of 0 is given for non-explosive eruptions. The volcanic impact on the atmosphere is measured by the so-called volcanic dust veil index (DVI). DVI is a numerical index that quantifies the impact of a particular volcanic eruption's release of dust and aerosols over the years following the event, especially the impact on the Earth's energy balance [Lamb, 1985]. This index is based on a review of the observational, empirical, and theoretical studies of the possible impact on climate of volcanic dust veils. The methods used to calculate the DVI have been intercalibrated to give a DVI of 1000 for the eruption of Krakatoa in 1883.

The El Chichon volcano (17.36°N, 266.77°E) erupted on March 28, 1982 with VEI=5. The weighted DVI was 366 [Mann et al, 2010] for the year 1982, the largest in the last 150 years before this event. The Ti drop in 1982 mentioned at the beginning of Section 3 (Figure 3, left panel) happened to be around the same time frame of the El Chichon volcano eruption. The drop reached 70-90K at 250-350 km. We notice that Ti at St

Santin (44.6°N, 2.2°E) experienced the same drop in 1982 for 50K at 350km [Donaldson et al., 2010].

The enormous eruption of the Mountain Pinatubo volcano (15.13°N, 120.35°E) took place on April 2, 1991 with a VEI=6. The weighted DVI was 500 for 1991, 375 for 1992 and 250 for 1993. These large VEIs in years 1991-1993 may be also contributed by another major volcano eruption at Mountain Hudson (45.90°S, 287.04°E) in August-October, 1991 with VEI=5, immediately following the Pinatubo eruption earlier in the year. These effects, with their primary origins in the Asia and South America sectors, were not very noticeable in the Millstone Hill Ti data till 1992, and maximized in the Ti data in 1993 when the Ti decreased by 50-60 K at 250-350 km. The time delay (by ∼2 years) in the ionospheric temperature response to the dramatically enhanced weighted VEI is very similar to the impact function determined for the LIDAR observation of the mesospheric temperature data for the Pinatubo volcano events [She et al, 1998].

The forth major volcano eruption during this 1968-2006 period was at St. Helens (46.20°N, 237.82°E) starting in March 1980 with a VEI=5. The weighted DVI was merely 51 for 1980, which is too low to produce any important influence in the atmosphere. No clear anomalous Ti behavior was found for this year. Even if a 2-year time delay in the impact function is real, the Ti drop in 1982 could hardly be contributed by this small weight DVI event.

The connection between the atmospheric temperature and volcano eruptive activities has been explored previously. In general, the volcanic aerosol causes a decrease in the mean global temperature because the droplets both absorb solar radiation and scatter it back into space. This temperature decrease was observed during the El Chichon and

Pinatubo eruptions (see, e.g., Rampino and Self [1984]). But for high altitudes of the atmosphere, a stratospheric temperature increase on a global scale was found to follow the Mountain Pinatubo volcano eruption [Labitzke and McCormick, 1992], and a mesopause temperature warming at a midlatitude site was also found following the same eruption [She et al, 1998]. The increased absorption due to mass loading of sulfuric acid aerosol into the stratosphere can possibly cause an immediate and *regional* temperature increase, however, the complex atmospheric dynamics can lead to global consequences in a delayed time. Interestingly, observations of the OH rotational temperature (a proxy for atmospheric kinetic temperatures at 87 km), made over the 18 year period between 1980-1998 at an European midlatitude site, showed clear coolings with minima around 1981 and 1992-1993 in the annual mean temperatures [Bittner et al., 2002]. The timing and cooling are very much similar to those for Ti presented here.

The ISR observations at Millstone Hill presented here and at St. Santin shown by Donaldson et al. [2010] provide multiple cases showing sizable Ti drops on the order of 50-100K in the F2 region heights, corresponding to those major volcano eruptions. The causal relationship between the upper thermospheric temperature drops and volcano eruptions, however, remains speculative, but their effect on low atmosphere is more definite as shown in literature and thus, if it shall finally arrive at the thermobase, the thermosphere can be disturbed. Nevertheless, a number of open questions concerning how low atmospheric responses propagated upward to impact the upper atmospheric thermal budget exist and need to be answered in more dedicated future studies.

5. Summary

This paper provides a comprehensive view of the long-term trend in the ionospheric ion temperature over the 200-550 km height range, as measured by the incoherent scatter radar at Millstone Hill over an extraordinary long time span between 1968-2006. This study extends a prior work [Zhang et al., 2011] which focused on midday only. These new results are highly necessary as inter-comparisons among ISR Ti, satellite density and modeling are emerging, and the latter two results have been typically averages throughout different local times. This study addresses the trend variability with local time, season, solar activity, and magnetic activity, in addition to discussion on potential impacts of the secular change in Earth's magnetic field locally on Millstone Hill. Results from this study can be summarized as the following:

(1) A gross average of the Ti trend in the heights where Ti$\sim$Tn (200-350 km), regardless of solar activity, season, local time and magnetic activity (low to moderate levels), is $\sim$ -4K/decade over 1968-2006, close to the Tn estimate based on the satellite neutral density data. In comparison, for the same 39-year time span and altitude range but at local noon, the cooling trend was found to be -11.6K/decade by Zhang et al. [2011]. In that same study, a cooling was registered as -21K/decade for the same conditions (local noon in 1968-2006) except for a higher altitude of 375 km. This differs from a cooling of -47K/decade determined for the same altitude and local time but over a shorter and later time span in 1978-2007 in Holt and Zhang [2008], indicating much stronger cooling in the later years than in the earlier years over the entire 1968-2007 period. There exists considerable height dependency and day-night, solar minimum-solar maximum, and magnetic activity variations in the trend, and these have to be carefully addressed for inter-comparisons.

In particular, the stronger cooling trend at high altitudes may be caused in part by less energy transfer from electrons due to the long-term electron density reduction at high altitudes.

(2) The cooling trend is strong during the day, and very weak during the night with a large apparent warming at low altitudes. The solar cycle dependency is prominent for both daytime and nighttime, with more cooling at solar minimum and less cooling or apparent warming at solar maximum. The strongest cooling below 375 km occurs not at the lowest level of the F107 flux, but around 90-120. The substantial day-night and solar maximum-solar minimum differences can lead to the gross average trend significantly reduced from the strong cooling under conditions of midday for solar minimum. No consistent and substantial seasonal dependency across different heights was found.

(3) There appears more cooling toward high magnetic activity, but this dependency is too weak to ascribe the observed upper atmospheric cooling to the long-term magnetic activity increase during the time period being examined.

(4) We speculate that a fraction of the observed cooling trend over Millstone Hill may be contributed by gradually shifting away from the sub-auroral region, as part of the secular change in Earth's magnetic fields. This effect can be seen in a theoretical simulation.

(5) In the 39-year long series of Ti data record, two anomalous Ti drops were found in 1982 and 1993 respectively. We speculate on their connection to volcano eruptions in 1982 (El Chichon) and 1991 (Pinatubo), a topic worth further investigation.

Acknowledgments. We thank members of the Haystack Observatory Atmospheric Sciences Group for assembling and maintaining the Madrigal Database. William L. Oliver was responsible for verifying the 2-pulse data and maintaining it for many years prior to its inclusion in the Madrigal Database. We also thank W. L. Oliver for his inspiration on potential influences of the 1982 volcano activity and his comments on the F107 effect during our many discussions on Millstone Hill observations. Discussions with Liying Qian have been very helpful for our deeper understanding of the NO cooling effect. Ingrid Cnosses kindly supplied her CMIT simulation data [Cnossen and Richmond, 2013] for this study, and allowed us to generate Figure 12 in the paper. Both I. Cnosses and W. L. Oliver read the draft manuscript and offered very valuable comments and suggestions. The Millstone Hill incoherent scatter radar is supported by the US National Science Foundation (NSF) Geospace (Upper Atmospheric) Facilities Program under a cooperative Agreement between NSF and Massachusetts Institute of Technology (MIT). This work is also supported by the NSF award AGS-1042569 to MIT.

References

Akmaev, R. A. (2012), On estimation and attribution of long-term temperature trends in the thermosphere, *J. Geophys. Res.,* 117, A09321, doi:10.1029/2012JA018058.

Akmaev, R. A., V. I. Fomichev (1998), Cooling of the mesosphere and lower thermosphere due to doubling of CO_2, *Ann. Geophys.,* 16, 1501-1512.

Akmaev, R. A., V. I. Fomichev, and X. Zhu (2006), Impact of middle-atmospheric composition changes on greenhouse cooling in the upper atmosphere, *J. Atmos. Sol. Terr. Phys.,* 68, 1879-1889, doi:10.1016/j.jastp.2006.03.008.

Bauer, P., P. Waldteufel, and D. Alcayde (1970), Diurnal variations of the atomic oxygen density and temperature determined from incoherent scatter measurements in the ionospheric F region,*J. Geophys. Res.,* 75(25), 48254832, doi:10.1029/JA075i025p04825.

Bittner, M., Offermann, D., Graef, H. H., Donner, M., and Hamilton, K. (2002), An 18-year time series of OH rotational temperatures and middle atmosphere decadal variations. *J. Atmos. Sol. Terr. Phys.,* 64(8-11), 11471166. doi:10.1016/S1364-6826(02)00065-2

Bremer, J. (2008), Long-term trends in the ionospheric E and F1 regions, *Ann. Geophys.*, 26, 11891197, doi:10.5194/angeo-26-1189-2008.

Clilverd, M. A., T. G. C. Clark, E. Clarke, and H. Rishbeth (1998), Increased magnetic storm activity from 1868 to 1995, *J. Atmos. Sol. Terr. Phys.*, 60, 10471056, doi:10.1016/S1364-6826(98)00049-2.

Cnossen, I., and A.D. Richmond (2008), Modelling the effects of changes in the Earth's magnetic field from 1957 to 1997 on the ionospheric hmF2 and foF2 parameters, *J. Atmos. Sol. Terr. Phys.,* 70, 1512-1524.

Cnossen, I. (2012), Climate change in the upper atmosphere, in *Greenhouse Gases: Emission, Measurement, and Management*, edited by G. Liu, pp. 315336, InTech, Rijeka, Croatia, ISBN 978-953-51-0323-3.

Cnossen I. and A. D. Richmond (2013), Changes in the Earth's magnetic field over the past century: effects on the ionosphere-thermosphere system and solar quiet (Sq) magnetic variation, *J. Geophys. Res.,* doi:10.1029/2012JA018447, in press.

Danilov, A. D. (2008), Critical frequencies foF2 as an indicator of trends in thermospheric dynamics, *J. Atmos. Sol. Terr. Phys.,* 48, 775-786.

Danilov, A. D. (2012), Long-term trends in the upper atmosphere and ionosphere (a review). Geomagnetism and Aeronomy, 52(3), 271291. doi:10.1134/S0016793212030036

Donaldson, J. K., T. J. Wellman, and W. L. Oliver (2010), Long-term change in thermospheric temperature above Saint Santin, *J. Geophys. Res.,* 115, A11305, doi:10.1029/2010JA015346.

Emmert, J. T., J. L. Lean, and J. M. Picone (2010), Record-low thermospheric density during the 2008 solar minimum, *Geophys. Res. Lett.,* 37, L12102, doi:10.1029/2010GL043671.

Emmert, J. T., J. M. Picone, J. L. Lean, and S. H. Knowles (2004), Global change in the thermosphere: Compelling evidence of a secular decrease in density, *J. Geophys. Res.,* 109, A02301, doi:10.1029/2003JA010176.

Emmert, J. T., J. M. Picone, and R. R. Meier (2008), Thermospheric global average density trends, 1967–2007, derived from orbits of 5000 near-Earth objects, *Geophys. Res. Lett.,* 35, L05101, doi:10.1029/2007GL032809.

Goncharenko, L., and S.-R. Zhang (2008), Ionospheric signatures of sudden stratospheric warming: Ion temperature at middle latitude, Geophys. Res. Lett., 35, L21103, doi:10.1029/2008GL035684.

Hedin, A.E. (1987), MSIS 86 thermospheric model, *J. Geophys. Res.,* 92, 4649-4662.

Holt, J. M., and S. R. Zhang (2008), Long-term temperature trends in the ionosphere above Millstone Hill, *Geophys. Res. Lett.,* 35, L05813, doi:10.1029/2007GL031148.

ionospheric models based on Millstone Hill incoherent scatter radar data, *Geophys. Res. Lett.,* 29, 1207, doi:10.1029/2002GL014678.

Keating, G. M., R. H. Tolson, and M. S. Bradford (2000), Evidence of long-term global decline in the Earth's thermospheric densities apparently related to anthropogenic effects, *Geophys. Res. Lett.,* 27, 1523-1526.

International Association of Geomagnetism and Aeronomy, Working Group V-MOD (2010), International Geomagnetic Reference Field: the eleventh generation, *Geophys. J. Int.*, 183, 3, 1216-1230, DOI: 10.1111/j.1365-246X.2010.04804.x.

Labitzke, K. and M. P. McCormick (1992), Stratospheric temperature increases due to Pinatubo aerosols, *Geophys. Res. Lett.,* 19(2), 207210, doi:10.1029/91GL02940.

Lamb, H. H., Volcanic Loading (1985): the dust veil index, CDIC Numberic Data Collection, NDP-013, DOI: 10.3334/CDIAC/atg.ndp013.

Laštovička, (2012), On the role of ozone in long-term trends in the upper atmosphere-ionosphere system, *Ann. Geophys.,* 30, 811-816, doi:10.5194/angeo-30-811-2012

Laštovička, J., S. C. Solomon, and L. Qian (2012), Trends in the Neutral and Ionized Upper Atmosphere, *Space Sci. Rev.*, 168, 113-145, 10.1007/s11214-011-9799-3.

Mann, M.E., E.P. Gille, R.S. Bradley, M.K. Hughes, J.T. Overpeck, F.T. Keimig, and W.S. Gross (2000), Global temperature patterns in past centuries: An interactive presentation, IGBP Pages/World Data Center for Paleoclimatology Data Contribution Series No. 2000-075. NOAA/NGDC Paleoclimatology Program, Boulder CO, USA.

Marcos, F. A., J. O. Wise, M. J. Kendra, N. J. Grossbard, and B. R. Bowman (2005), Detection of a long-term decrease in thermospheric neutral density, *Geophys. Res. Lett.,* 32, L04103, doi:10.1029/2004GL021269.

Marsh, D. R., S. C. Solomon, and A. E. Reynolds (2004), Empirical model of nitric oxide in the lower thermosphere, *J. Geophys. Res.,* 109, A07301, doi:10.1029/2003JA010199

Mikhailov, A. V., and D. Marin (2001), An interpretation of the foF2 and hmF2 long-term trends in the framework of the geomagnetic control conception, *Ann. Geophys.,* 19, 733-748.

Mursula, K., and D. Martini (2006), Centennial increase in geomagnetic activity: Latitudinal difference and global estimates, *J. Geophys. Res.,* 111, A08209, doi:10.1029/2005JA011549.

Newhall, C.G., and Self, S. (1982), The volcanic explosivity index (VEI): An estimate of explosive magnitude for historical volcanism, *J. Geophys. Res.,* 87, 1231-1238.

Oliver, W. L. (1979), Incoherent scatter radar studies of the daytime middle thermosphere, *Ann. Geophys.,* 35, 121-139.

Rampino, M.R., and S. Self (1984), The atmospheric effects of El Chichon, *Sci. Amer.*, 250(1), 48-57.

Qian, L., R. G. Roble, S. C. Solomon, and T. J. Kane (2006), Calculated and observed climate change in the thermosphere, and a prediction for solar cycle 24, *Geophys. Res. Lett.,* 33, L23705, doi:10.1029/2006GL027185.

Qian, L., S. C. Solomon, R. G. Roble, and T. J. Kane (2008), Model simulations of global change in the ionosphere, *Geophys. Res. Lett.,* 35, L07811, doi:10.1029/2007GL033156.

Qian, L., J. Laštovička, R. G. Roble, and S. C. Solomon (2011), Progress in observations and simulations of global change in the upper atmosphere, J. Geophys. Res., 116, A00H03, doi:10.1029/2010JA016317, [printed 117(A2), 2012].

Rishbeth, H. (1990), A greenhouse effect in the ionosphere, *Planet. Space Sci.*, 38, 945-948.

Roble, R. G., and R. E. Dickinson (1989), How will changes in carbon-dioxide and methane modify the mean structure of the mesosphere and thermosphere, *Geophys. Res. Lett.,* 16, 1441-1444.

She, C. Y., S. W. Thiel, and D. A. Krueger (1998), Observed episodic warming at 86 and 100 km between 1990 and 1997: Effects of Mount Pinatubo Eruption, *Geophys. Res.*

Lett., 25(4), 497500, doi:10.1029/98GL00178.

Solomon, S. C., T. N. Woods, L. V. Didkovsky, J. T. Emmert, and L. Qian (2010), Anomalously low solar extreme-ultraviolet irradiance and thermospheric density during solar minimum, *Geophys. Res. Lett.,* 37, L16103, doi:10.1029/2010GL044468.

Solomon, S. C., L. Qian, L. V. Didkovsky, R. A. Viereck, and T. N. Woods (2011), Causes of low thermospheric density during the 2007-2009 solar minimum, *J. Geophys. Res.,* 116, A00H07, doi:10.1029/2011JA016508.

Walsh, P. L., and W. L. Oliver (2011), Is thermospheric long-term cooling due to CO2 or O3, *Ann. Geophysica*, 29, 17791782, doi:10.5194/angeo-29-1779-2011.

Wang, W., M. Wiltberger, A. G. Burns, S. C. Solomon, T. L. Killeen, N. Maruyama, and J. G. Lyon (2004), Initial results from the coupled magnetosphere-ionosphere-thermosphere model: thermosphere-ionosphere responses, *J. Atmos. Sol. Terr. Phys.,* 66, 1425, doi:10.1016/j.jastp.2004.04.008.

Wang, W. B., J. H. Lei, A. G. Burns, M. Wiltberger, A. D. Richmond, S.C. Solomon, T. L. Killeen, E. R. Talaat, and D. N. Anderson (2008), Ionospheric electric field variations during a geomagnetic storm simulated by a coupled magnetosphere ionosphere thermosphere (CMIT) model, *Geophys. Res. Lett.,* 35(18), L18105.

Wiltberger, M., W. Wang, A. G. Burns, S. C. Solomon, J. G. Lyon, and C. C. Goodrich (2004), Initial results from the coupled magnetosphere-ionosphere-thermosphere model: magnetospheric and ionospheric responses, J. Atmos. Solar-Terr. Phys., 66, 1411, doi:10.1016/j.jastp.2004.04.026.

Yue, X., W. Wan, L. Liu, B. Ning, and B. Zhao (2006), Applying artificial neural network to derive long-term foF2 trends in the Asia/Pacific sector from ionosonde observations, *J. Geophys. Res.,* 111, A10303, doi:10.1029/2005JA011577.

Zhang, S.-R. and J. M. Holt (2008), Ionospheric variability from an incoherent scatter radar long-duration experiment at Millstone Hill, *J. Geophys. Res.,* 113, A03310, doi:10.1029/2007JA012639

Zhang, S.-R., J. M. Holt, P. J. Erickson, F. D. Lind, J. C. Foster, A. P. van Eyken, Y. Zhang, L. J. Paxton, W. C. Rideout, L. P. Goncharenko, and G. R. Campbell (2005), October 2002 30-day Incoherent Scatter Radar Experiments at Millstone Hill and Svalbard and Simultaneous GUVI/TIMED Observations, *Geophys. Res. Lett.,* 32, L01108, doi:10.1029/2004GL020732.

Zhang, S.-R., J. M. Holt, A. P. van Eyken, M. McCready, C. Amory-Mazaudier, S. Fukao, and M. Sulzer (2005), Ionospheric climatology and model from long-term databases of worldwide incoherent scatter radars, Eos Trans. AGU, 86(18), Jt. Assem. Suppl., Abstract SA52A-03.

Zhang, S.-R., J. M. Holt, A. M. Zalucha, and C. Amory-Mazaudier (2004), Midlatitude ionospheric plasma temperature climatology and empirical model based on Saint Santin incoherent scatter radar data from 1966-1987, *J. Geophys. Res.,* 109, A11311, doi:10.1029/2004JA010709.

Zhang, S.-R., J. M. Holt, and J. Kurdzo (2011), Millstone Hill ISR observations of upper atmospheric long-term changes: Height dependency, *J. Geophys. Res.,* 116, A00H05, doi:10.1029/2010JA016414, [printed 117(A2), 2012].

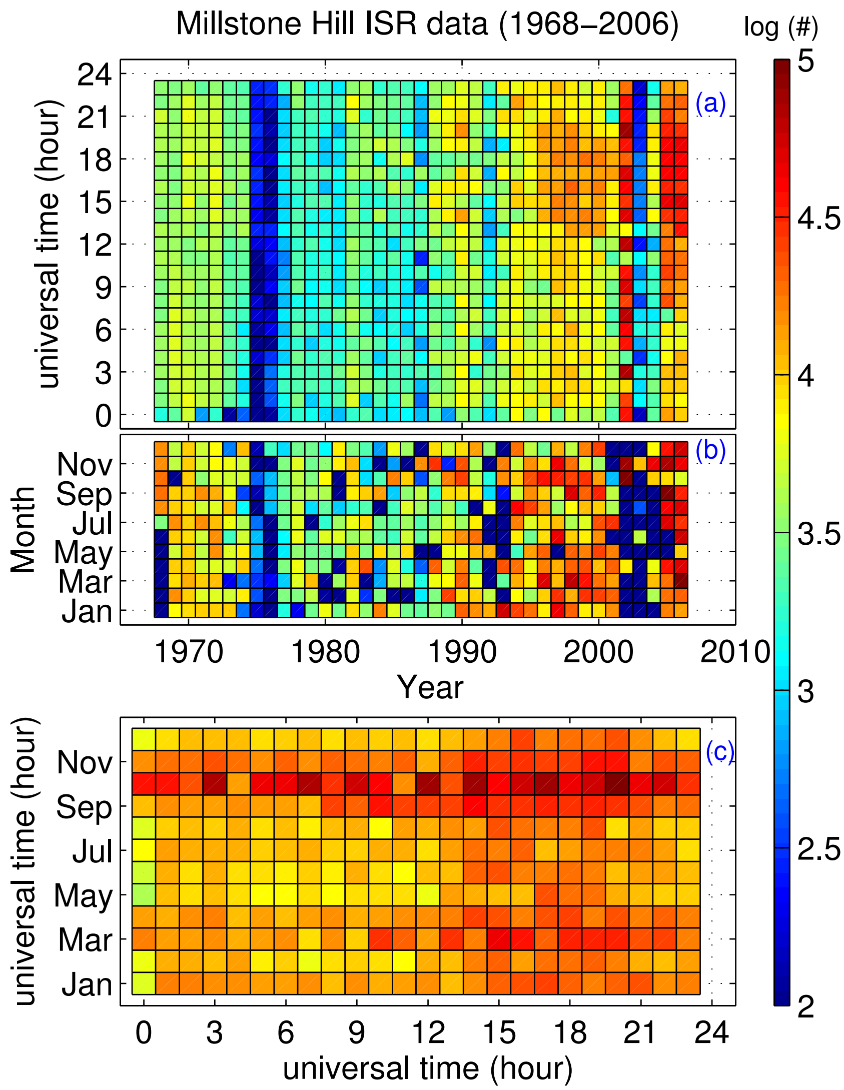

Figure 1. Data distribution as a function of year and universal time (the top panel, a), as a function of year and month (the middle panel, b), and as a function of universal time and month (the bottom panel, c).

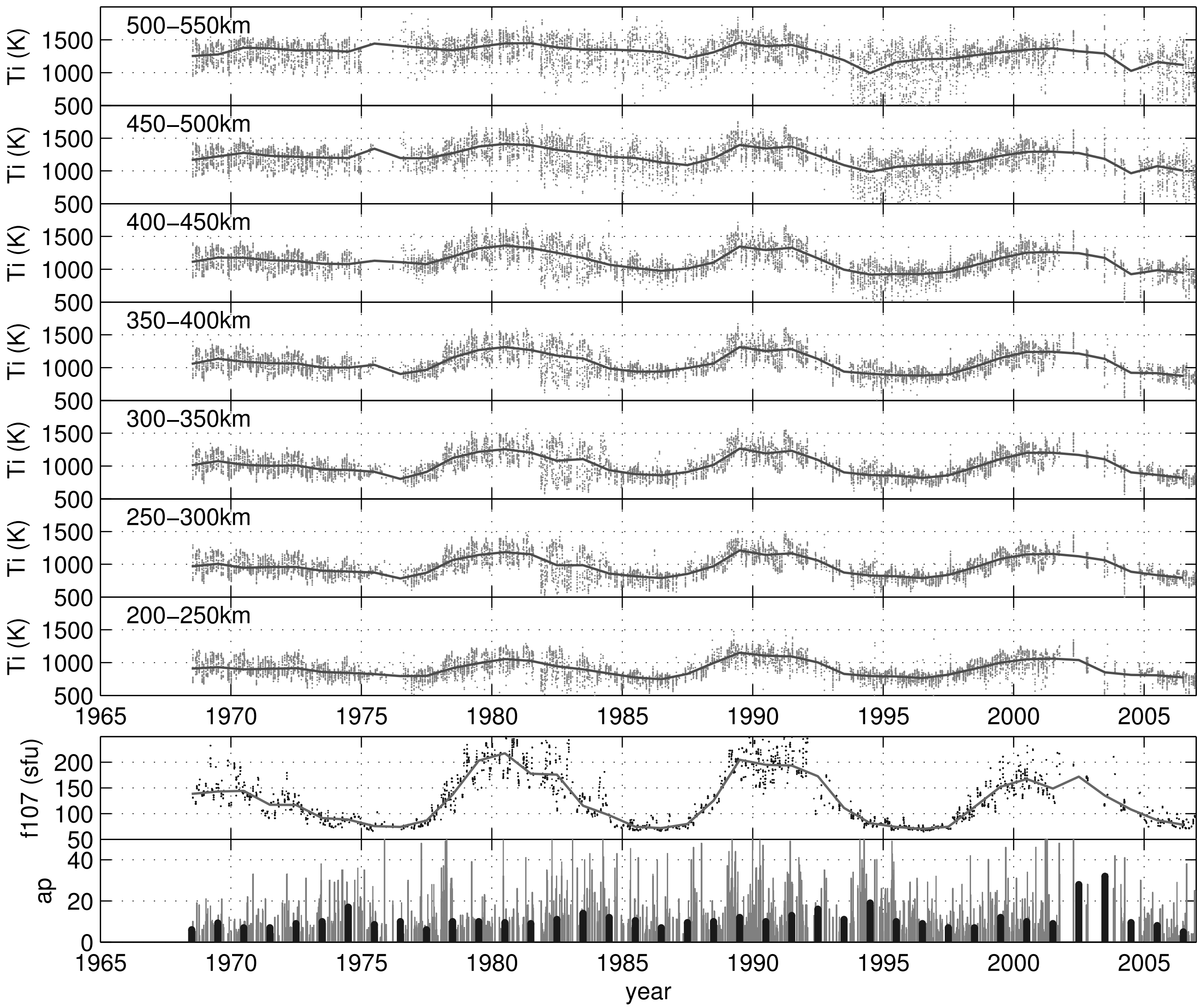

Figure 2. Long-term observational Ti data obtained with data binning in local time and height and averaging over a month (top panel), and corresponding F107 (middle panel) and Ap index (bottom panel). The solid lines in the top and middle panels and the black bars in the bottom panels are yearly averages.

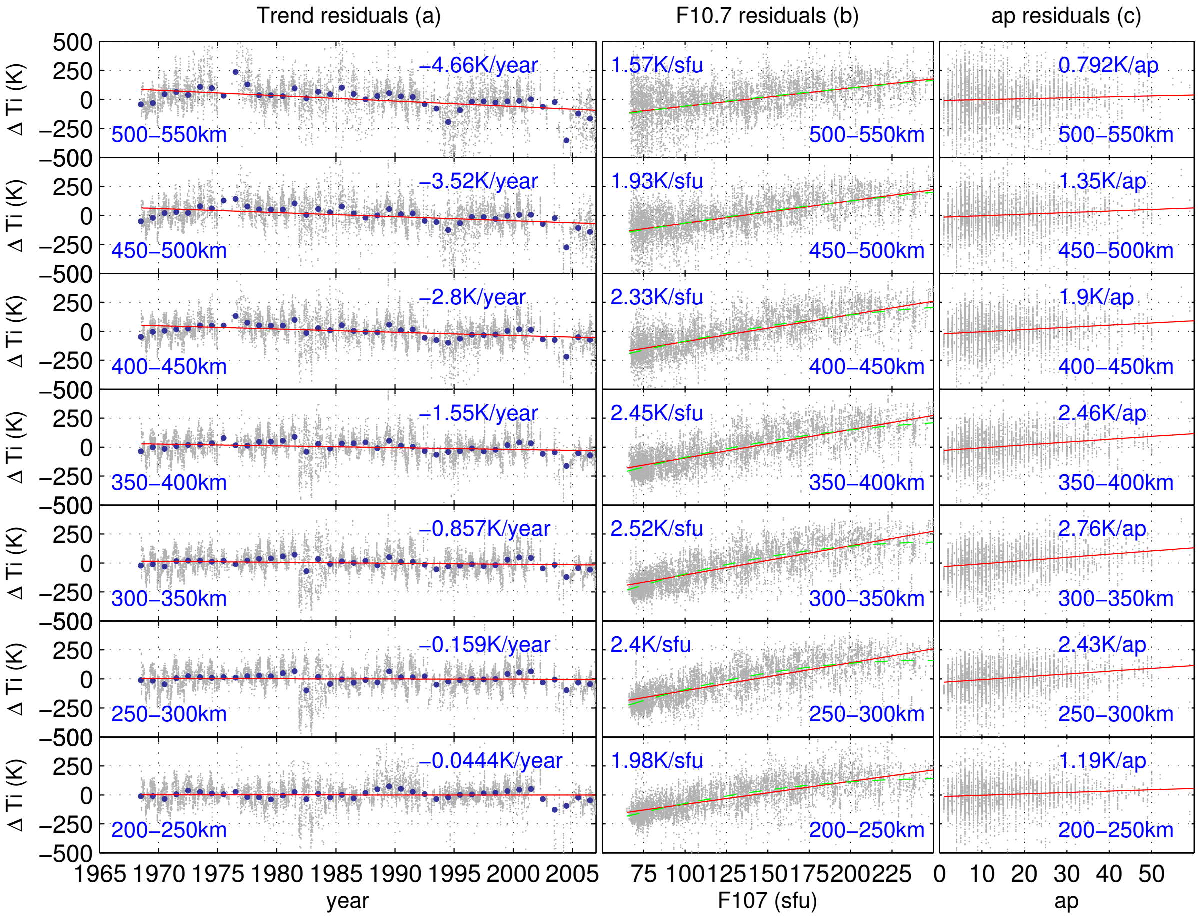

Figure 3. Ti residuals calculated by subtracting geophysical terms from the observed data for different altitude bins as a function of time of the day, month and year. The trend residuals (a) are a result of subtracting all terms except for the trend one, the F107 residuals (b) are a result of subtracting all terms except for the F107 terms, and the Ap residuals are a result of subtracting all terms except for the Ap one. See text for more details. Red lines in each panel are a linear fit to the gray dots which are residuals for a given local time, month and year. The green line (only in panel b) is a fit to a parabolic function. Solid dots (only in panel a) are yearly averages calculated from different local times and months.

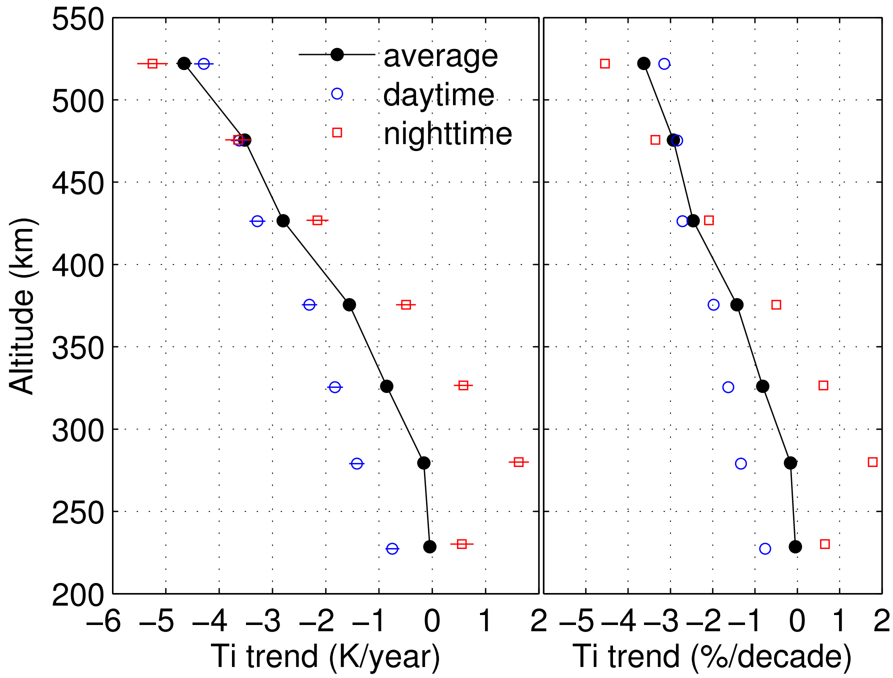

Figure 4. Height profiles of the Ti trend for daytime (12±4 LT, circles), nighttime (0±4LT, squares), and over the entire day (0-24LT, solid dots). Error bars are χ^2-scaled standard deviations for the calculated linear trends. The left panel shows trends in the K/year unit and the right panel shows trends in the %/decade unit, defined as the Ti trend per decade divided by the average Ti.

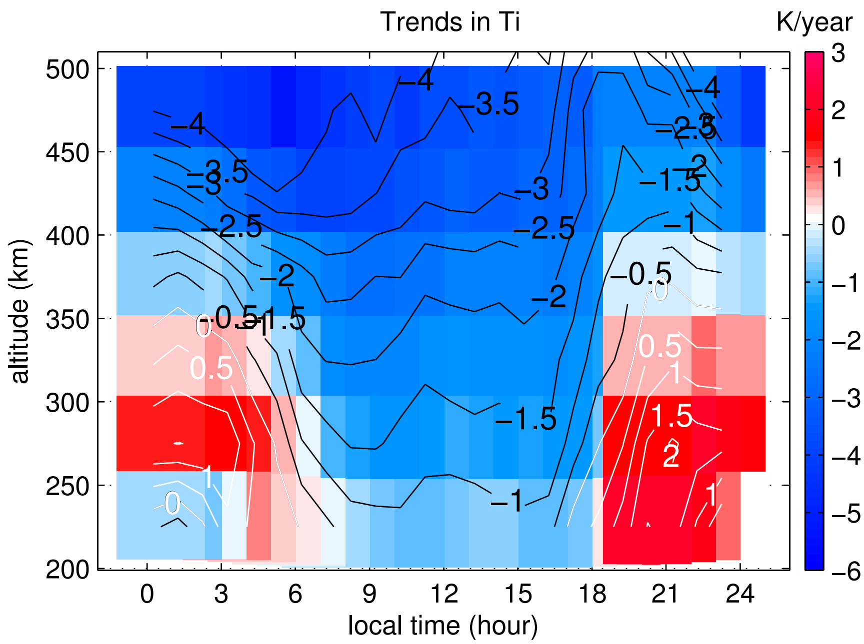

Figure 5. Diurnal vs height variations of the Ti trend. Contours are marked with trend values at a 0.5 unit interval between -4 and 2 K/year. Overlapped is the color shaded contours.

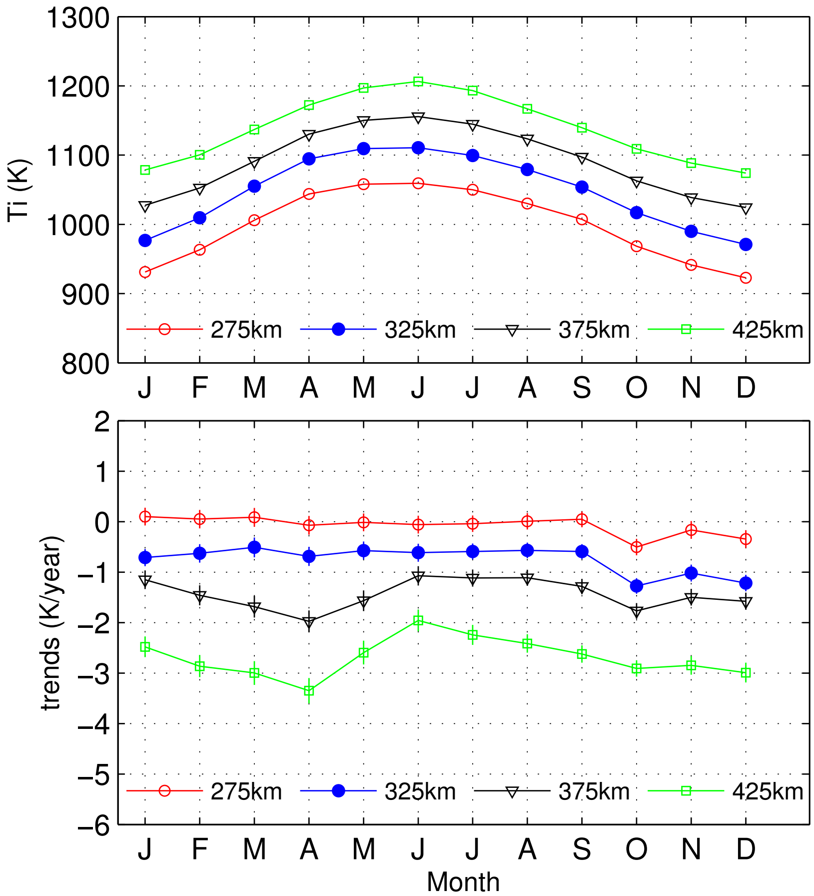

Figure 6. Seasonal variation of the Ti trend at various heights in the F2 region (bottom), and the corresponding median Ti (topside). Both Ti trend and median Ti are calculated within a running 3-month seasonal bin size from data with different local times and years. Error bars are χ^2-scaled standard deviations for the calculated linear trends.

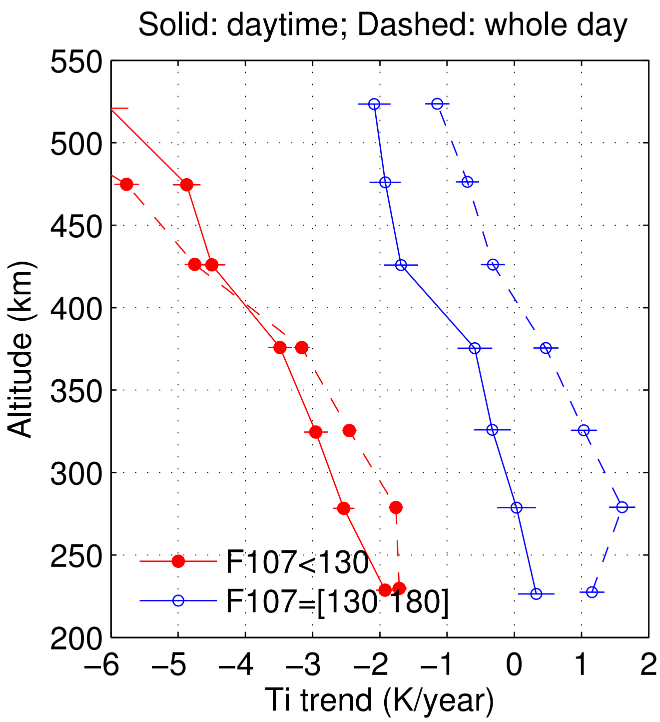

Figure 7. Height profiles of the Ti trends derived from trend residuals for two solar activity levels: F107<130 (low solar activity), and 130 <F107<180 (high solar activity). The solid lines are results for daytime (12±4 LT) data only while the dashed lines are daily averages for all data regardless local time. Error bars are χ^2-scaled standard deviations for the calculated linear trends.

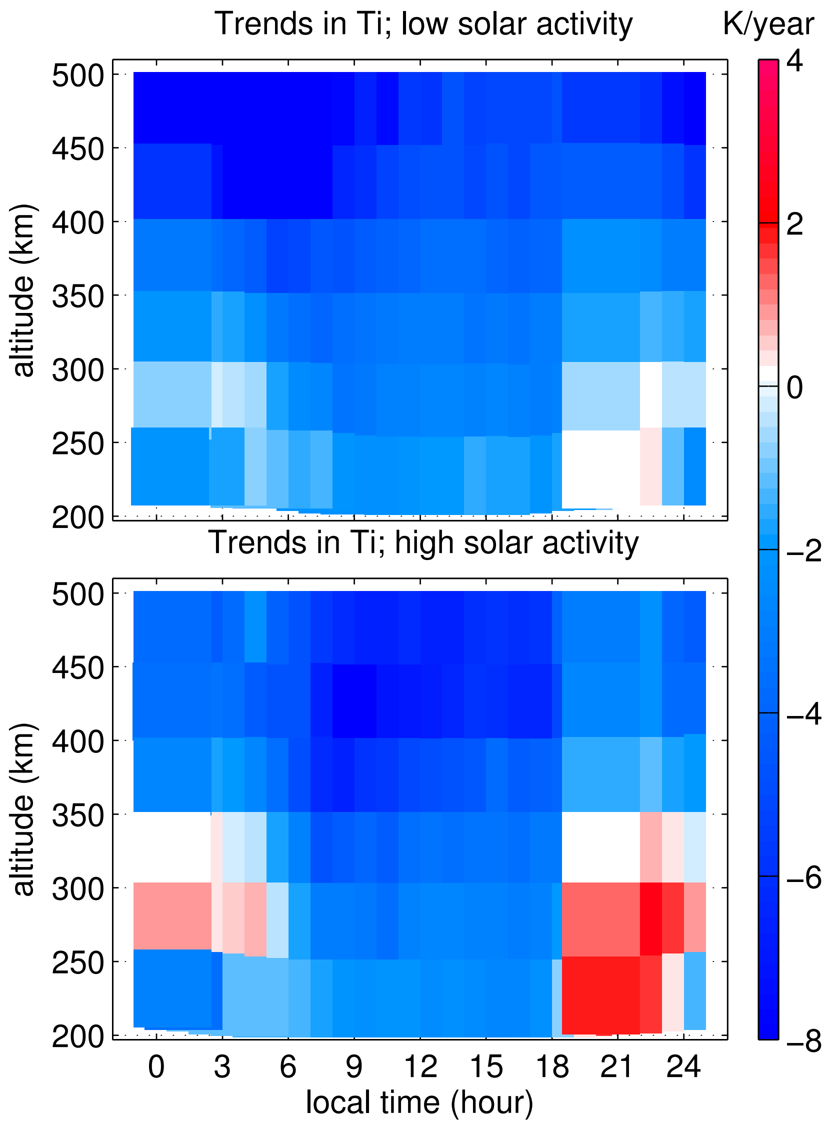

Figure 8. Long-term trends in Ti as a function of height and local time for low solar activity (F107<130; upper panel) and for high solar activity (130 <F107<180; bottom panel).

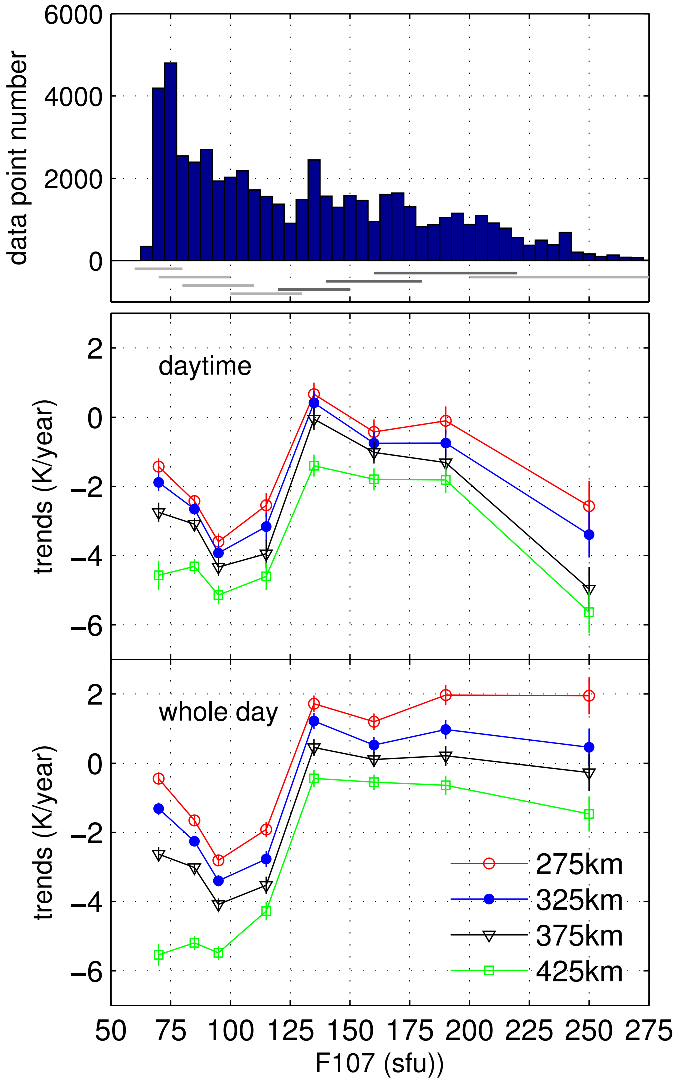

Figure 9. Dependency of the Ti trend on F107. F107 histogram is shown with a bin width of 5 sfu in the top panel, the next two panels show the trends as a function of F107 for daytime (12±4LT; middle panel) and for the whole day (bottom panel). These trend values are determined for trend residuals within particular F107 ranges, which are indicated by the horizontal bars at the bottom of the top panel. Error bars shown with the trend are χ^2-scaled standard deviations for the linear trend fitting.

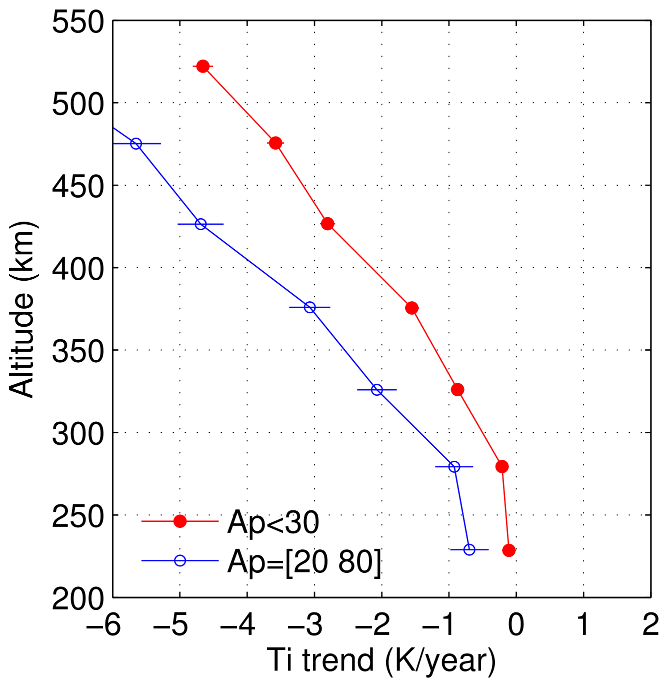

Figure 10. Height profiles of Ti trends derived from trend residuals for two magnetic activity levels: Ap <30 (low activity), and 20<Ap<80 (high activity). Error bars are χ^2-scaled standard deviations for the calculated linear trends.

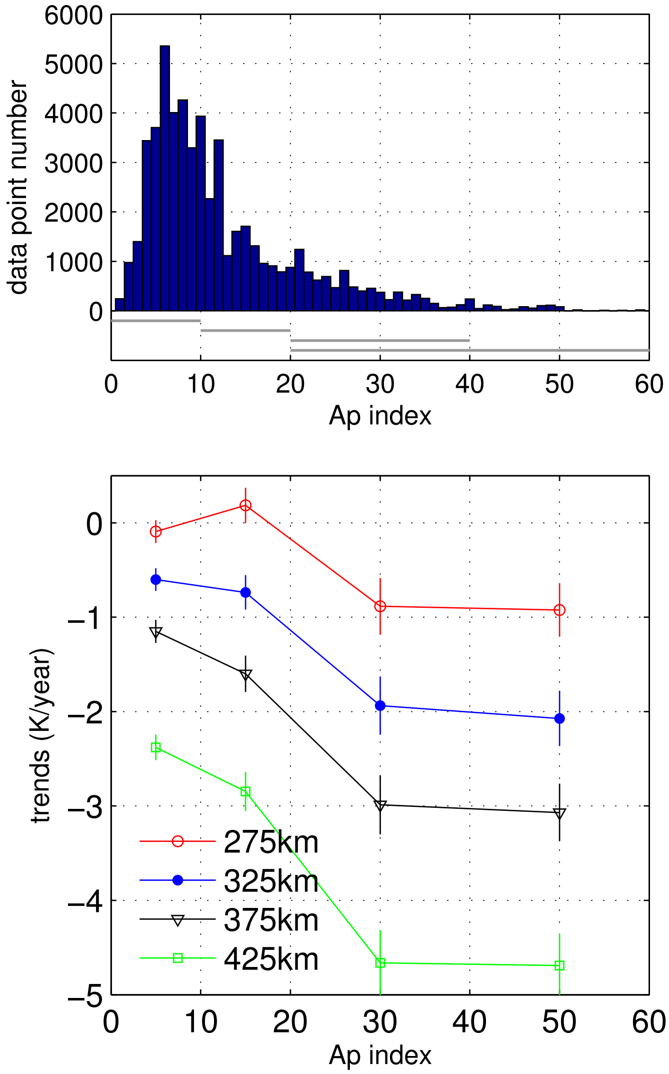

Figure 11. Dependency of the Ti trend on Ap. Ap histogram is shown in the top panel with a bin width of 1 unit. Trends as a function of Ap for the F region heights are given in the bottom panel. These trend values are determined for trend residuals within particular Ap ranges, which are indicated by the horizontal bars at the bottom of the top panel. Error bars shown with the trend are χ^2-scaled standard deviations for the linear trend fitting.

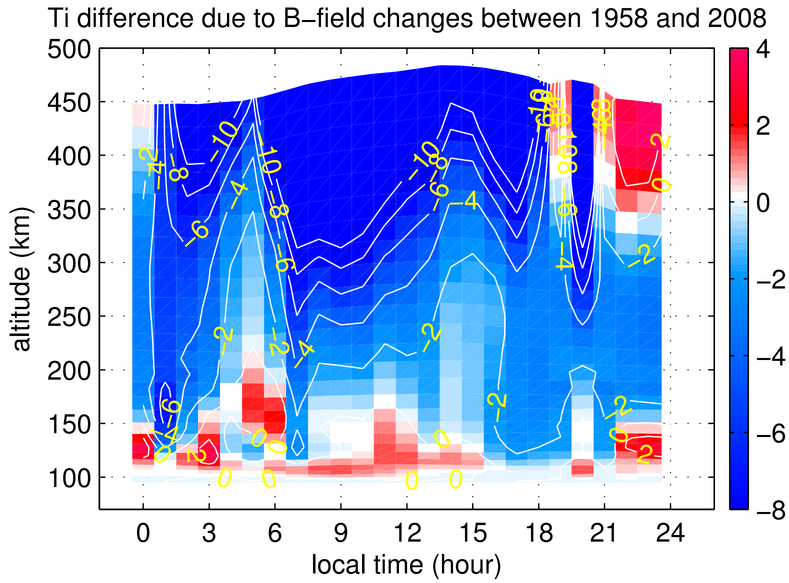

Figure 12. A CMIT simulation of Ti changes due to the secular change in magnetic fields between 1958 and 2008 as specified by the IGRF model. Ti differences are shown as a function of local time and height. The simulation runs were carried out for 15 days around spring equinox under solar minimum conditions. Mean values over the 15 day period for each run are first calculated before the differences are taken. Blue color represents a cooling trend.